# OBSERVABLE PROPERTIES OF DOUBLE-BARRED GALAXIES IN *N*-BODY SIMULATIONS

Juntai Shen[1,3] and Victor P. Debattista[2,4]

[1] McDonald Observatory, The University of Texas at Austin, 1 University Station, C1402, Austin, TX 78712, USA; shen@astro.as.utexas.edu
[2] Astronomy Department, University of Washington, Seattle, WA 98195, USA; debattis@astro.washington.edu

## ABSTRACT

Although at least one quarter of early-type barred galaxies host secondary stellar bars embedded in their large-scale primary counterparts, the dynamics of such double-barred galaxies are still not well understood. Recently we reported success at simulating such systems in a repeatable way in collisionless systems. In order to further our understanding of double-barred galaxies, here we characterize the density and kinematics of the *N*-body simulations of these galaxies. This will facilitate comparison with observations and lead to a better understanding of the observed double-barred galaxies. We find the shape and size of our simulated secondary bars are quite reasonable compared to the observed ones. We demonstrate that an authentic decoupled secondary bar may produce only a weak twist of the kinematic minor axis in the stellar velocity field, due to the relatively large random motion of stars in the central region. We also find that the edge-on nuclear bars are probably not related to boxy peanut-shaped bulges which are most likely to be edge-on primary large-scale bars. Another kinematic feature often present in our double-barred models is a ring-like feature in the fourth-order Gauss–Hermite moment $h_4$ maps. Finally, we demonstrate that the non-rigid rotation of the secondary bar causes its pattern speed to not be derived with great accuracy using the Tremaine–Weinberg method. We also compare with observations of NGC 2950, a prototypical double-barred early-type galaxy, which suggest that the nuclear bar may be rotating in the opposite sense as the primary.

*Key words:* galaxies: evolution – galaxies: kinematics and dynamics – galaxies: structure – stellar dynamics

*Online-only material:* color figures

## 1. INTRODUCTION

Double-barred (S2B) galaxies were first described over 30 years ago (de Vaucouleurs 1975). The *Hubble Space Telescope* has revealed secondary bars at the center of at least one quarter of early-type optically-barred galaxies (Erwin & Sparke 2002). Dynamically decoupled[5] secondary bars in S2B galaxies have been hypothesized to be a mechanism for driving gas past the inner Lindblad resonance (ILR) of primary bars, to feed the supermassive black holes that power active galactic nuclei (AGN; Shlosman et al. 1989).

The dynamics of secondary bars are still not well understood. The random apparent relative orientations of primary and secondary bars in nearly face-on galaxies points to dynamical decoupling (Buta & Crocker 1993; Friedli & Martinet 1993). But images alone cannot reveal much about how the two bars rotate through each other. Kinematic evidence of decoupling, using either gas or stars, is harder to obtain (Petitpas & Wilson 2002; Schinnerer et al. 2002; Moiseev et al. 2004). Indirect evidence for decoupling was claimed by Emsellem et al. (2001) based on rotation-velocity peaks inside the secondary bars. Conclusive, direct kinematic evidence for a decoupled secondary bar was obtained for NGC 2950 by Corsini et al. (2003, hereafter CDA03) who showed, using the method of Tremaine & Weinberg (1984), that the primary and secondary bars cannot be rotating at the same pattern speed.

Simulations offer the best way to understand double-barred systems. However, the decoupled nuclear bars that formed in early simulations did not last long. For example, the most

long-lived nuclear bar in Friedli & Martinet (1993) lasted for less than two turns of the primary bar, corresponding to about 0.4 Gyr, which is far too short to explain the observed abundance of nested bars. Furthermore, their models usually require substantial amounts of gas to form and maintain these nuclear bars. Heller et al. (2007a, 2007b) reported that nested bars form in a quasi-cosmological setting, but the amplitudes of the bars also seem to weaken rapidly after most of the gas has formed stars (Heller et al. 2007a, Figure 2). Petitpas & Wilson (2004) found that four out of 10 double-barred galaxies contain very little molecular gas in the nuclear region. These clues suggest that large amounts of molecular gas may not be necessary to maintain central nuclear bars. Rautiainen et al. (2002) reported that a secondary bar forms in a collisionless *N*-body simulation, although their secondary bar had a "vaguely spiral shape."

On the side of orbital studies, Maciejewski & Sparke (1997, 2000) discovered a family of loop orbits that may form building blocks of long-lived nuclear stellar bars (also Maciejewski & Athanassoula 2007). Their studies are very important for understanding double-barred galaxies, but their models are not fully self-consistent, since nested bars in general cannot rotate rigidly through each other (Louis & Gerhard 1988). So fully self-consistent *N*-body simulations are still needed to check if their main results still hold when the non-rigid nature of the bars is taken into account.

Recently, Debattista & Shen (2007, hereafter DS07) demonstrated that long-lived secondary bars can form in purely collisionless *N*-body simulations when a rotating pseudobulge is introduced in their model. The nuclear bars in their work are distinct bars, and do not have a spiral shape. They showed that the behavior of their models was in good agreement with the loop-orbit predictions of Maciejewski & Sparke (2000).

---

[3] Harlan J. Smith Fellow.
[4] Brooks Prize Fellow; current address: Centre For Astrophysics, University of Central Lancashire, Preston, UK PR1 2HE.
[5] In this context, by decoupled we mean only that $\Omega_s \neq \Omega_p$, where $\Omega_s$ ($\Omega_p$) is the pattern speed of the secondary (primary) bar.

In this report we analyze the photometric and kinematic properties of high-resolution models in detail. Our theoretical results here can also be compared to the observed two-dimensional kinematics of some double-barred galaxies to achieve a better understanding of the dynamics of the secondary bars.

## 2. MODELS

The simulations presented in this paper are all collisionless. The model setup is very similar to that of DS07. As in DS07, the formation of the secondary bar is induced by a rotating pseudobulge. We focus on three simulations: run D which formed a long-lasting double-barred system due to an initially rotating bulge, run S in which only a single bar formed with an initially unrotating bulge component, and run NB where there is no bulge component initially. It is worth stressing that the only difference in the setup of run D and run S is the bulge rotation, which is responsible for the formation of secondary bars in our models. Our high-resolution simulations consist of live disk and bulge components in a rigid-halo potential. We restrict ourselves to rigid halos to allow higher mass resolution in the nuclear regions to study the complicated co-evolution of the two bars without the additional evolution introduced by the halo. The rigid halos used in this study are all logarithmic potentials $\Phi(r) = \frac{1}{2}V_h^2 \ln \left(r^2 + r_h^2\right)$. We set $V_h = 0.6$ and $r_h = 15$ in all runs. We employed about four times more particles than the runs published in DS07 to better analyze the photometric and kinematic properties; Runs D and S have $4.8 \times 10^6$ equal mass particles, with $4 \times 10^6$ in the disk and the rest in the bulge. Run NB has $4 \times 10^6$ in the disk only, since there is no bulge.

The initial disks in our simulations all have exponential surface densities with scale-length $R_d$, mass $M_d$, vertical scale height $0.1R_d$, and Toomre-$Q \simeq 2$. The bulge was generated using the method of Prendergast & Tomer (1970) as described in Debattista & Sellwood (2000), where a distribution function is integrated iteratively in the global potential until convergence. In both run D and run S the bulge has mass $M_b = 0.2M_d$ and we used an isotropic King model distribution function. The bulge truncation radius is $0.9R_d$ in both run D and run S. The bulge set up this way is nonrotating. We introduce bulge rotation in run D by simply reversing the velocities of bulge particles with negative angular momenta, which is still a valid solution of the collisionless Boltzmann equation. The bulges in run D and run S are flattened by the disk potential initially, and remain so at later times. The initial kinematic ratio $(V_p/\bar{\sigma})_*$ in run D is about 1, which is in the regime of oblate isotropic rotators (Binney 1978). We have also run simulations with nuclear disks in place of the bulges and these give results in broad agreement with those here. A full description of these models will be presented elsewhere.

We use $R_d$ and $M_d$ as the units of length and mass, respectively, and the time unit is $\left(R_d^3/GM_d\right)^{1/2}$. If we scale these units to the physical values $M_d = 2.3 \times 10^{10}\ M_\odot$ and $R_d = 2.5$ kpc, then the unit of time is 12.3 Myr. We use a force resolution (softening) of 0.01, which scaled to the above physical units and corresponds to 25 pc. These simulations were evolved with a three-dimensional cylindrical polar grid code (Sellwood & Valluri 1997). This code expands the potential in a Fourier series in the cylindrical polar angle $\phi$; we truncated the expansion at $m = 8$. Forces in the radial direction are solved for by direct convolution with the Green's function, while the vertical forces are obtained by fast Fourier transform. We used grids measuring $N_R \times N_\phi \times N_z = 58 \times 64 \times 375$. The vertical spacing of the

grid planes was $\delta z = 0.01R_d$. Time integration used a leapfrog integrator with a fixed time step $\delta t = 0.04$.

## 3. PHOTOMETRY

### 3.1. Shape of the Secondary Bar

Figure 1 shows the surface density contours and images of the double-barred run D, and single-barred runs S and NB, the latter of which does not have an initial bulge component. From Figure 1 we see that for run D the secondary bar shows up in both the disk and bulge components. All three large-scale bars appear qualitatively similar to each other in both the face-on and edge-on views.

When viewed side-on, the large-scale bar appears to be boxy/peanut-shaped, regardless of whether or not an initial live bulge is included or if a secondary bar is present. The formation of a boxy/peanut-shaped bulge from disks via bending instabilities has been studied extensively with *N*-body simulations (e.g., Combes et al. 1990; Raha et al. 1991; Bureau & Athanassoula 2005; Debattista et al. 2005; Martinez-Valpuesta et al. 2006; Debattista et al. 2006). Figure 1 does not show any obvious influence of the secondary bar on the overall boxy/peanut-shaped side-on appearance of a large-scale bar. So it is quite unlikely that most box-shaped bulges are edge-on nuclear bars, as speculated by Kormendy & Kennicutt (2004) as a possibility of explaining boxy bulges. This is hardly surprising as the small size of the secondary bar makes its side-on signatures, if any, easily masked by the primary. A caveat may be that the boxiness in Figure 1 does not cover a range as wide as that in Debattista et al. (2006). Also note that the boxy part is smaller than the primary bar (regardless of double-barred or single-barred) as a whole (see Shen & Sellwood 2004; Kormendy & Kennicutt 2004; Martinez-Valpuesta et al. 2006; Debattista et al. 2006; Athanassoula & Beaton 2006).

Figure 2 shows the projected system (at $t = 405$ when the two bars are nearly perpendicular) with an ordinary orientation: the system is inclined at $i = 45°$ with the line of nodes (LON) of $\psi_{\rm nuc} = 45°$ relative to the secondary bar major axis. The surface density image and contours resemble many observed double-barred systems, such as NGC 2950, even though we did not deliberately set out to match it.

### 3.2. Size Relation of the Two Bars

Figure 3 shows radial variations of $m = 2$ Fourier amplitude and phase for run D at $t = 400$. Figure 4 shows the ellipticity and position angle (P.A.) profiles of ellipses fitted with IRAF for the same data as in Figure 3 (we use log scale for the radius to be consistent with what observers usually adopt). There are four popular methods for determining the semimajor axis $a_B$ of a bar, as summarized by O'Neill & Dubinski (2003) and Erwin (2005). For convenience, we denote the primary bar as B1 and the secondary bar as B2.

1. The bar end is measured by extrapolating half-way down the slope on the $m = 2$ amplitude plot (Figure 3(a)). We find $a_{B1} \sim 2.3$, $a_{B2} \sim 0.4$, the B2/B1 bar length ratio is about $\sim 0.17$.
2. The bar end is measured when the $m = 2$ phase deviates from a constant by $10°$ (Figure 3(b)). We find $a_{B1} \sim 2.1$, $a_{B2} \sim 0.4$, the B2/B1 bar length ratio is about $\sim 0.19$.
3. The bar end is measured at the peak of the fitted ellipticity profiles (e.g., Marinova & Jogee 2007; Menéndez-Delmestre et al. 2007), which is shown in Figure 4(a). We
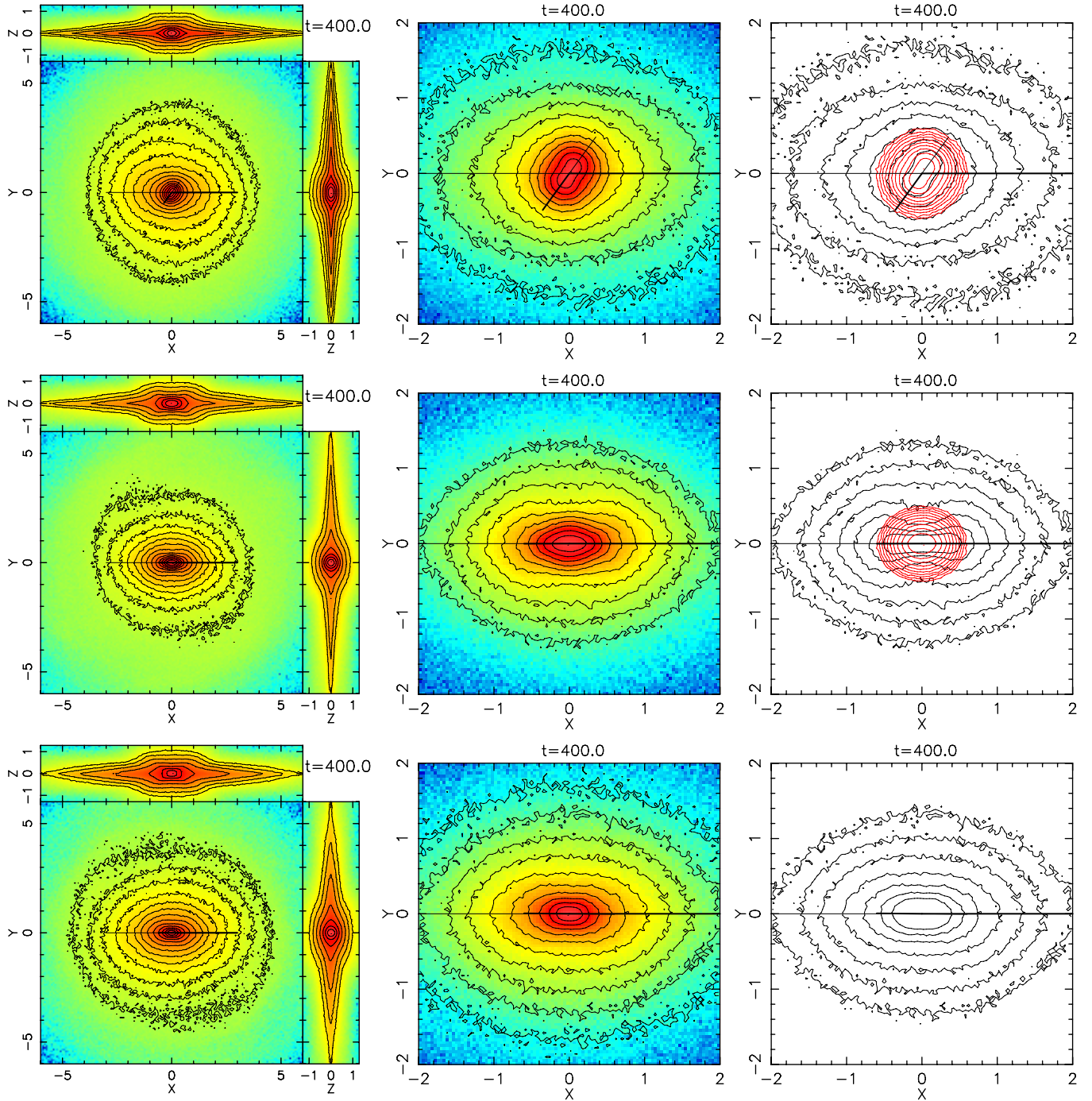
**Figure 1.** Three-dimensional surface density of three runs. In each row, from left to right, panels are for the large-scale total stellar distribution, central zoom-in of total stellar distribution, separate disk (dark) and bulge (red) surface density contours, respectively. (a) Top row: the canonical run with a secondary bar formed (run D); (b) middle row: the run with an unrotating bulge, which formed only a single bar (run S); (c) bottom row: the run without a bulge (run NB). The contours in the $x$–$y$ plane are separated by half dex, while in edge-on projections they are spaced more sparsely to avoid contour overcrowding.

(A color version of this figure is available in the online journal.)

find $a_{B1} \sim 1.7$, $a_{B2} \sim 0.2$, the B2/B1 bar length ratio is about $\sim 0.12$.

4. The bar end is measured when the P.A. of fitted ellipses deviates from a constant by $10°$ (Figure 4(b)). We find $a_{B1} \sim 2.3$, $a_{B2} \sim 0.4$, the B2/B1 bar length ratio is about $\sim 0.17$.

Methods 1, 2, and 4 yield consistent values of the bar lengths and length ratios. We found that method 3 tends to give a lower value of bar lengths than the other three methods, as shown in

O'Neill & Dubinski (2003). Although these methods have some uncertainties in measuring the bar lengths, the length ratio of the two bars is in the range of 0.12–0.19 (in particular methods 1, 2, and 4 give a consistent narrow range of 0.17–0.19). This result is in good agreement with the typical observed length ratio of local S2B systems (median ratio $\sim 0.12$, see Erwin & Sparke 2002; Erwin 2004; Lisker et al. et al. 2006). Note that we expect that the length of the secondary cannot be too large, otherwise the gravitational torque from the primary bar will inevitably twist
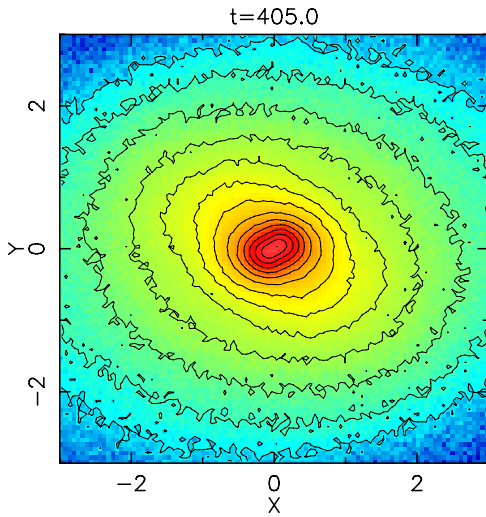
**Figure 2.** Run D at $t = 405$ projected to $i = 45°$ and $\psi_{\mathrm{nuc}} = 45°$ with all particles shown. The model bears a passing resemblance to NGC 2950 (Erwin & Sparke 2002).

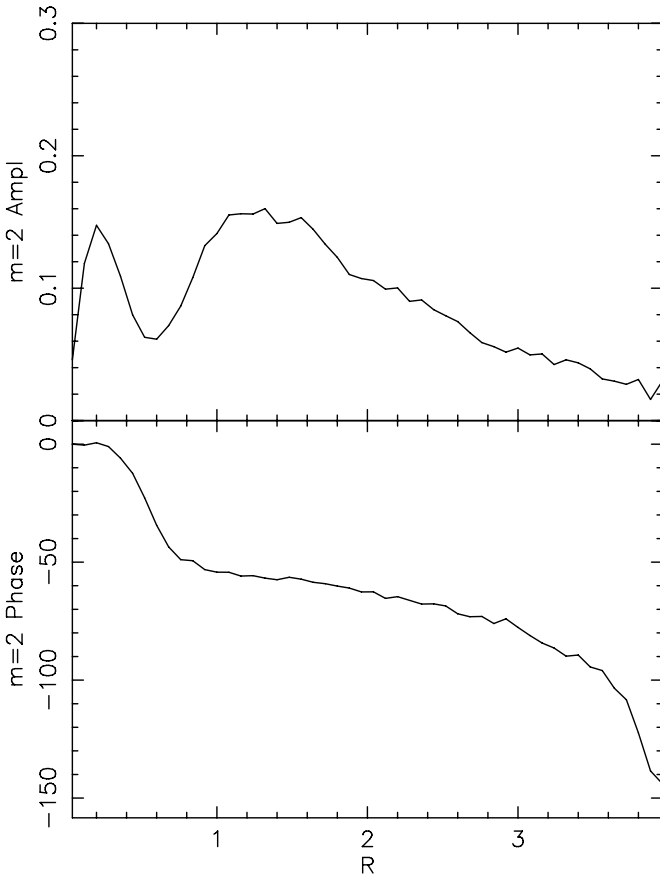(A color version of this figure is available in the online journal.)



**Figure 3.** Radial variations of the $m = 2$ Fourier amplitude and phase of all particles for run D at $t = 400$.
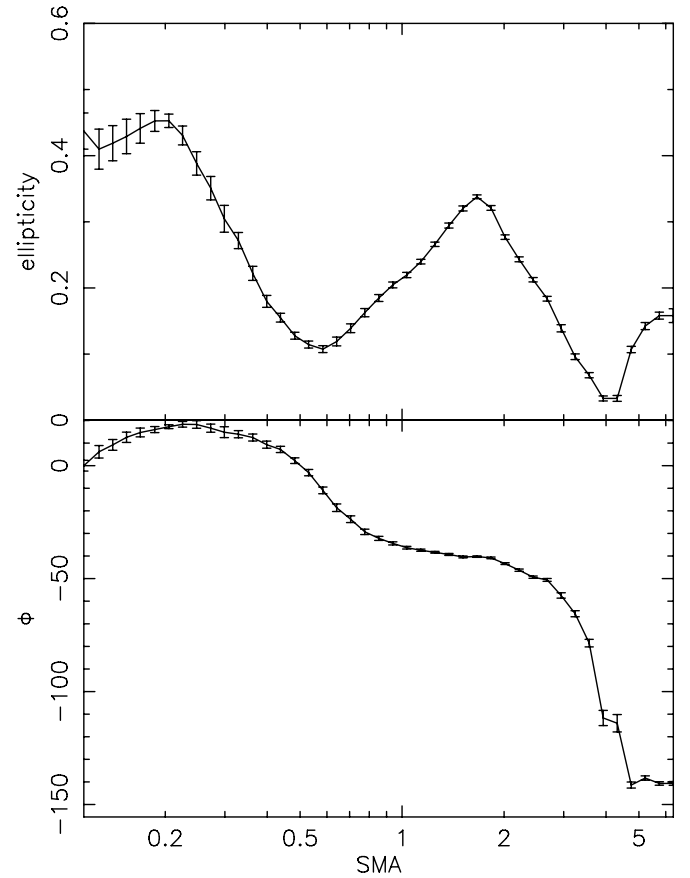


**Figure 4.** Ellipticity and P.A. as a function of semimajor axis of IRAF-fitted ellipses for run D at $t = 400$.

significant increase in central density following the formation of the large-scale bar which redistributes the disk particles. For run D, the central density profile along the primary bar major axis is no longer higher than that along the minor axis, due to the secondary bar orienting to a different direction from the primary bar. This minor axis over-density is, of course, even more pronounced when the two bars are perpendicular. This can be an important signature of photometrically confirming small secondary bars, especially when the central region is not well resolved. Variations in M/L are unlikely to mask this minor/major axis difference as density profiles are for roughly the same radial range. On the other hand, long-wavelength photometry is preferred to minimize the effects of dust. We do not find other significant differences in the face-on surface density profiles between run D and other runs without a secondary bar.

## 4. KINEMATICS

Figure 6 shows the behavior of the azimuthally averaged $\Omega$, $\Omega \pm \kappa/2$, and the location of the Lindblad resonances of the bars at around $t = 400$ for run D. As shown in DS07, the pattern speeds of the bars, especially that of the secondary, vary as they rotate through each other: the secondary bar rotates slower than average when the two bars are perpendicular, and faster when the bars are parallel. The pattern speed bands shown in Figure 6 reflect such variations. Clearly, the pattern speed of the secondary bar oscillates much more than that of the primary. The primary bar extends roughly to its corotation radius (CR) ($\sim 2.5$), consistent with the general expectation, and is therefore considered a fast bar (e.g. CDA03, Debattista & Williams 2004).

the secondary into alignment if they rotate at different pattern speeds.

### 3.3. Face-on Surface Density Profiles

Figure 5 shows the face-on surface density profiles along the major and minor axes of the primary bar in runs D, S, and NB. Compared with the initial profile of each run, there is a
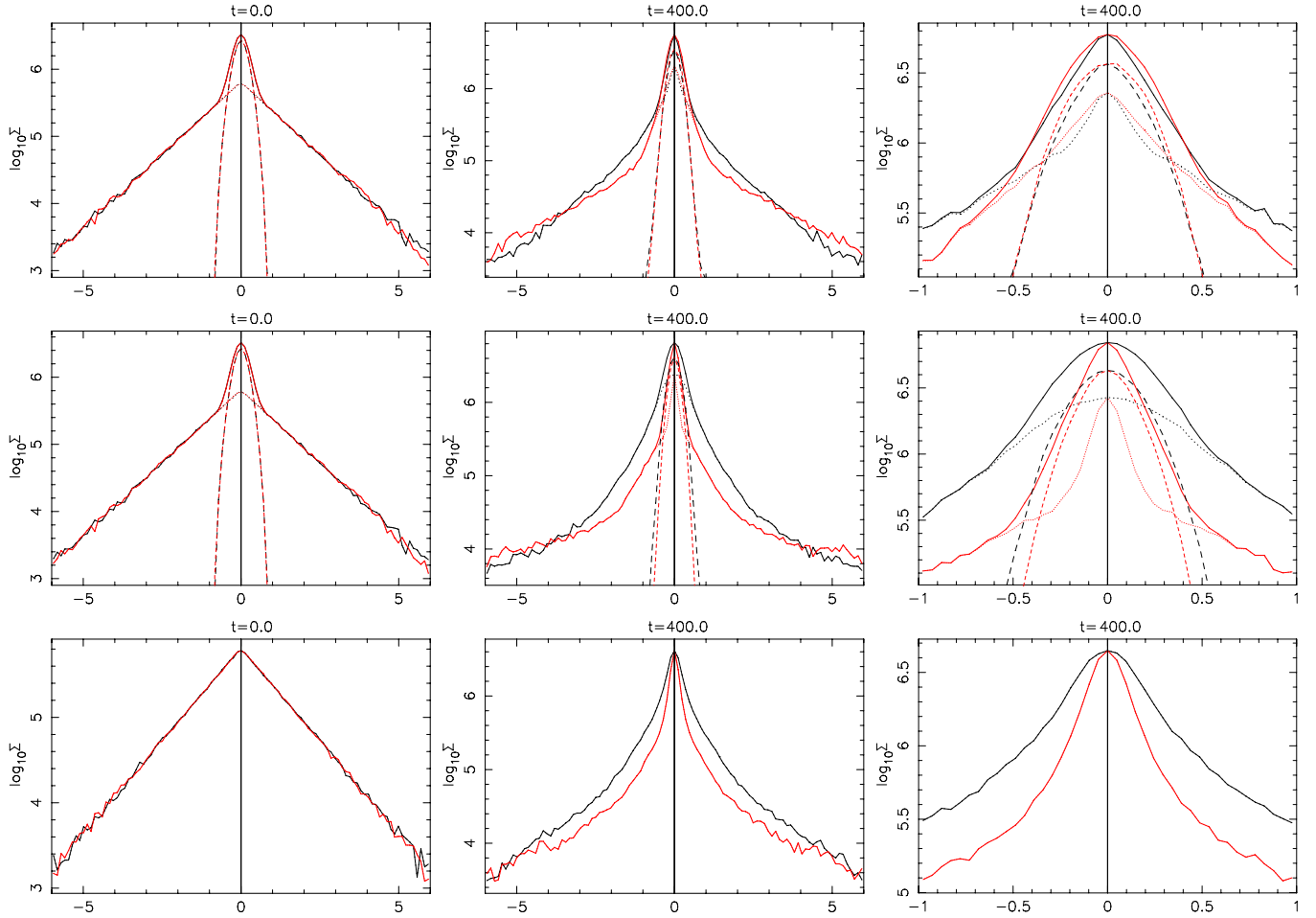
**Figure 5.** Face-on surface density profiles along major and minor axes of the primary bar for run D (top row), run S (middle row), and run NB (bottom row). For each row, from left to right: the surface density profile at $t = 0$, $t = 400$, and the close-up view of the inner region at $t = 400$, respectively. In all figures, solid lines are for surface density for all particles, dashed lines are for bulge particles only, and dotted lines are for disk particles only. The black and red curves are along the major and minor axes of the primary bar, respectively.

(A color version of this figure is available in the online journal.)

The secondary bar rotates faster than the primary bar. However, the secondary bar is much shorter than its shortest $R_{CR}$. In addition, even if the variation of the pattern speed is taken into account, the $R_{CR}$ of the secondary is not very close to the $R_{ILR}$ of the primary, if we use the same naive definition of $R_{ILR}$ as in Pfenniger & Norman (1990).[6] This is inconsistent with the CR–ILR coupling proposed to be a requirement for making secondary bars (e.g., Pfenniger & Norman 1990; Friedli & Martinet 1993).

Since the long-lasting secondary bars which form in our simulations generally do not extend to their CR, the kinematics of secondary bars differ from those of primary bars in at least this important detail. We here explore the kinematic observables of S2Bs in our simulations in more detail.

### 4.1. Line-of-Sight Velocity Distribution

We analyzed the line-of-sight velocity distribution (LOSVD) by measuring the mean velocity $\bar{v}$ and velocity dispersion $\sigma$. Departures from a Gaussian distribution are parameterized by Gauss–Hermite moments (Gerhard 1993; van der Marel & Franx

1993; Bender et al. 1994). The second-order term in such an expansion is related to the dispersion. Following Gerhard (1993) the third-order term $h_3$ and fourth-order term $h_4$ are defined as

$$h_n = \frac{\sqrt{4\pi}}{\Sigma} \int l(w) H_n(w) \exp^{(-1/2)w^2} \, dw$$

where $w = (v - \bar{v})/\sigma$, $n = 3$ or $4$, $H_3(w) = [1/(96\pi)^{1/2}](8w^3 - 12w)$, and $H_4(w) = [1/(768\pi)^{1/2}](16w^4 - 48w^2 + 12)$. For a particle model, the integral becomes a sum and $\Sigma$ is replaced by $N_p$, the number of particles in a bin. $h_3$ measures deviations that are asymmetric about the mean, while $h_4$ measures the lowest-order symmetric deviations from Gaussian (negative for a "flat-top" distribution, and positive for a more peaked one).

Another way to obtain $\bar{v}$, $\sigma$, $h_3$, and $h_4$ altogether is by $\chi^2$ fitting the velocity distribution directly with the combined Gauss–Hermite polynomials. We have verified that the kinematic values derived by directly fitting are in very good agreement with the calculated values used in Figures 7–9.

Figures 7(a)–(e) show surface density maps and the LOS stellar kinematics of run D at $t = 405$ when the two bars are almost perpendicular to each other. For comparison purpose Figure 7(f) is for run NB (run S is very similar to run NB, so it is not shown for brevity). As in Figure 2, we project the system to $i = 45°$ with the LON of $45°$ relative to the secondary bar major axis.

---

[6]   A cautionary note is that the $R_{ILR}$ read naively from Figure 6 serves just as a visual guide, because the $R_{ILR}$ determined this way is reliable only for weak bars, and is questionable for our strong bars (e.g., van Albada & Sanders 1982).
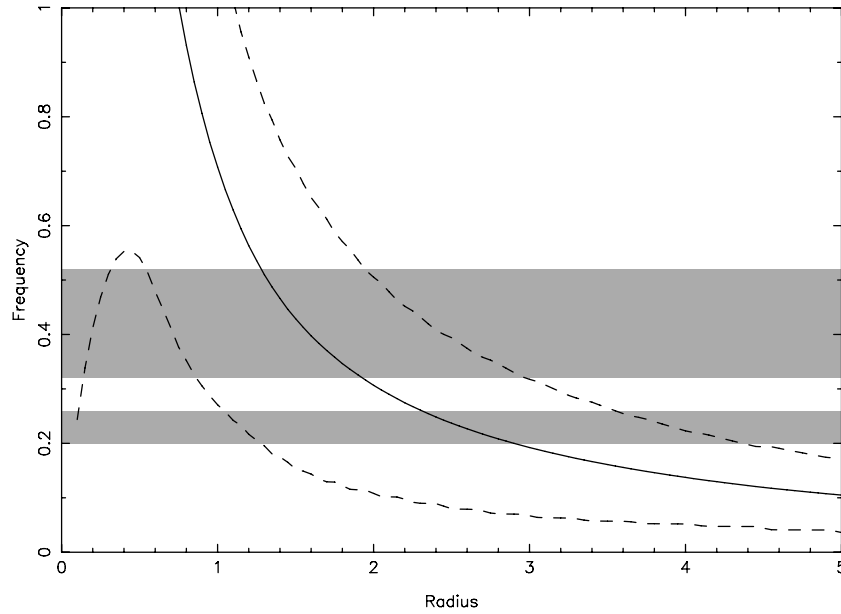
**Figure 6.** Frequencies as a function of radius at around $t = 400$ for run D, calculated based on the azimuthally averaged gravitational attraction. The full-drawn line shows the curve of the circular angular frequency $\Omega$ and the dashed curves mark $\Omega \pm \kappa/2$, where $\kappa$ is the epicyclic frequency. The two shaded bands show the oscillational ranges of the bar pattern speeds (the upper band is for the secondary bar and the lower one is for the primary).

The most striking feature in Figure 7 is that the twist of the kinematic minor axis (i.e. $v_{los} = 0$) in the secondary bar region is weak (see the mean velocity maps in Figure 7(b)–(e). The kinematic minor axis is almost perpendicular to the inclination axis, although there is a small but noticeable twisted pinch near the kinematic minor axis in the nuclear region. The weak central twist is mainly due to the relatively large velocity dispersion, especially in the central region (likewise at $t = 20$, when only the small nuclear bar exists, the stellar twist is stronger than at $t = 405$, but still quite small compared to the expected twist in gaseous kinematics). On the other hand, the twist of the kinematic major axis is more prominent in the central region. Moiseev et al. (2004) found the stellar kinematic minor axis hardly twists from the photometric minor axis in their sample with the most reliable kinematics, leading them to question whether nuclear photometric isophotal twists represent bona fide dynamically decoupled secondary bars. We demonstrate that an authentic decoupled secondary bar may indeed produce a very weak twist of the kinematic minor axis in the stellar velocity field. So a central stellar velocity map without a strong twist as in Moiseev et al. (2004) does not necessarily exclude the existence of a decoupled nuclear bar.

As a comparison, Figure 7(f) shows that the kinematic minor axis twist is slightly stronger for the single-barred run NB. Of course gas kinematics may show much more twisted features than the stellar data (e.g., Moiseev et al. 2004; Emsellem et al. 2006). However, the gas in the nuclear region is more prone to nongravitational forces like shocks, AGN jets, and outflows, so may not directly probe the underlying gravitational potential.

It is also worth noting that the $\sigma$ symmetry axis does not align with the secondary or the primary bars (also true for the single-bar run NB), which is consistent with what Moiseev et al. (2004) found.

Another interesting feature in Figure 7 is the $h_4 > 0$ ring encircling the secondary bar of run D. In Figure 8 we compare the $h_4$ images at typical times in run D, run S, and run NB. The $h_4$ ring is clearly present at various times in run D, regardless of the angle between the primary and secondary bars, whereas no clear $h_4$ ring is visible in the single-bar runs S and NB. We have verified that the $h_4$ ring shows up in most projections unless the inclination angle $i \gtrsim 50°$. We notice that the $h_4$ ring is absent at $t = 0$, so it is not set-in from the different initial conditions, but developed as the double bars form. Also the $h_4$ ring is absent in both the disk-particles-only and bulge-particles-only $h_4$ maps, so it must stem from the distribution of stars from two components with different $\sigma_{los}$. The $h_4$ ring will be explored further in a follow-up study.

### 4.2. Slit Kinematics

Figure 9 shows the evolution of the slit profiles along the major axis of the primary/secondary bar of run D as the secondary rotates through the primary bar, and slit profiles for run S. We notice that there is no central velocity dispersion ($\sigma$)-drop in our simulated double-barred systems. So the $\sigma$-drop (as found in Emsellem et al. 2001, 2006) is not a requirement, and is not always associated with the formation of a double-barred system. More likely $\sigma$-drops are just the signature of newly formed (therefore dynamically "cool") stars (Emsellem et al. 2001, 2006). Simulations have shown that a $\sigma$-drop can be produced in single-barred galaxies (Wozniak et al. 2003; Wozniak & Champavert 2006), so it is not necessarily a unique feature of double-barred systems.

In the case of a single bar (run S), $h_3$ in Figure 9(c) has relatively less features along the major axis of the large-scale bar in the nuclear region ($R \lesssim 0.2$); the $h_3$ correlation with $\overline{v}$ is an indication of the high-velocity tail created by the elongated orbits supporting the large-scale bar. On the other hand, in Figure 9(a) and 9(b), nuclear $h_3$ features are quite prominent at many times, like the $h_3$ anti-correlation with $\overline{v}$. These $h_3$ reversal features manifest the complex asymmetric LOS velocity distribution as the result of the decoupled secondary bar, probably due to the strong rotation in the central bulge region. However, we also found that such $h_3$ features are suppressed at some orientations and times.

The double $h_4$ peaks in both Figure 9(a) and 9(b) also confirm the existence of the $h_4$ ring we discussed in the last subsection.
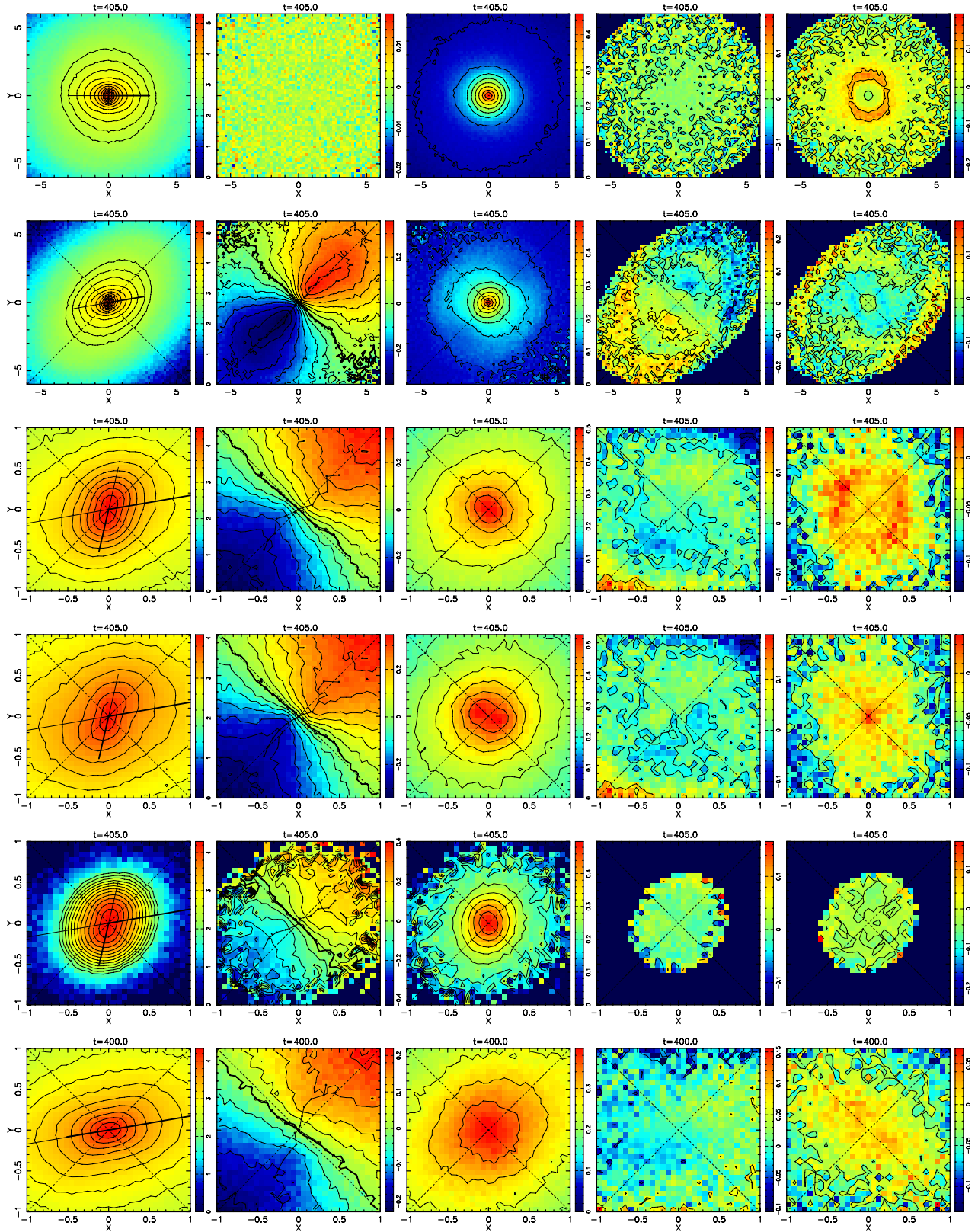
**Figure 7.** Photometric and kinematic maps of run D and run NB. For each row from left to right are the projected surface density, mean velocities ("spider diagrams"), velocity dispersion, $h_3$, and $h_4$ maps. (a) Row 1: run D at $t = 405$ face-on. (b) Row 2: run D at $t = 405$ inclined at $45°$ with the LON of $45°$ relative to the primary bar major axis. (c) Row 3: close-up views of run D at $t = 405$ projected the same way as (b). (d) Row 4: as in (c) but include disk particles only. (e) Row 5: as in (c) but include bulge particles only. (f) Row 6: run NB at $t = 400$ inclined at $45°$ with the LON of $45°$ relative to the (single) bar major axis. The corresponding fields for run S are similar to that of run NB, so they are not shown for brevity. The short and long straight line segments label the direction of the secondary and primary bars, respectively (note the length of the line segment does not represent the bar length). For the projected plot, one of the dashed lines represents the line of nodes ($45°$), while the other dashed line is the anti-LON ($135°$). In the mean velocity map, the line with the connected dots shows the rough position of the kinematic major axis, while the heavy solid curve is the zero-velocity curve (kinematic minor axis). The $h_3$ and $h_4$ analyses are not preformed in bins with less than 100 particles.

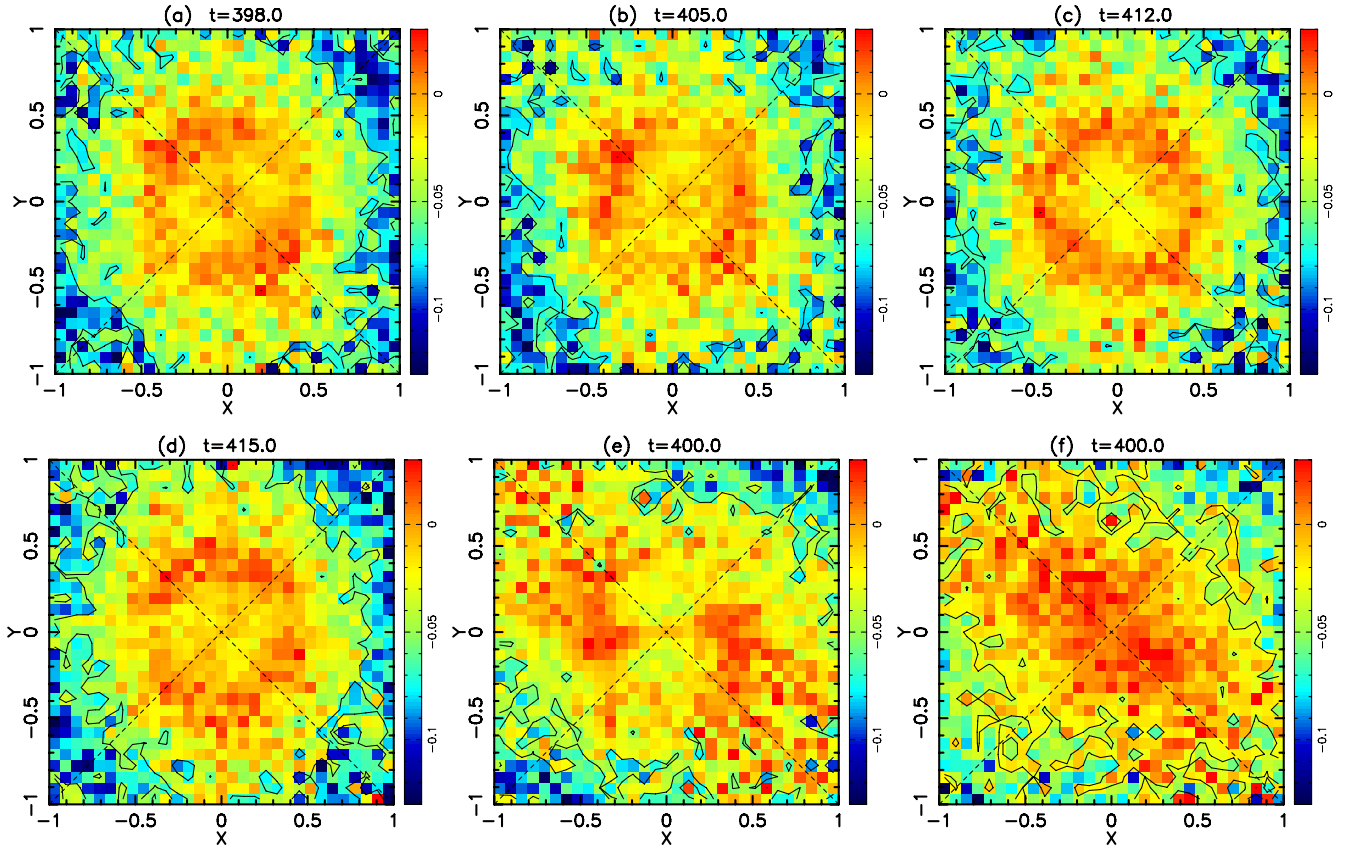(A color version of this figure is available in the online journal.)

**Figure 8.** Comparison of $h_4$ features in run D, run S, and run NB. Panels (a)–(f) are $h_4$ images for run D at $t = 398$ (two bars at 135°), run D at $t = 405$ (90°), run D at $t = 412$ (∼ 45°), run D at $t = 415$ (∼ 0°), run S at $t = 400$, and run NB at $t = 400$, respectively. The projection parameters are the same for all panels: $i = 45°$ with the LON of 45° relative to the primary bar major axis.

(A color version of this figure is available in the online journal.)

Although our secondary bar is clearly decoupled from the primary bar, the maximum of the rotational velocity does not occur in the nuclear region (Figure 9); instead the rotational velocity just rises smoothly past the region of the secondary bar (the half-length of the secondary bar is around 0.4, see Section 3.2). This is different from Emsellem et al. (2001), possibly indicating the location of the maximum of the rotational velocity is not a crucial factor for maintaining a nuclear bar.

## 5. PATTERN SPEED DETERMINATION

The dynamical state and evolution of barred galaxies is determined by the pattern speed of their bars. Knowledge of the pattern speeds of secondary bars may constrain mechanisms of their formation and evolution. Not much is yet known with certainty about secondary bar pattern speeds. Observationally, the only direct kinematic constraint on $\Omega_s$, based on the Tremaine–Weinberg (TW; Tremaine & Weinberg 1984) method, was obtained for NGC 2950 by CDA03, who showed that the primary and secondary bars cannot be rotating at the same rate. They further suggested that the secondary bar of NGC 2950 is either rotating faster or counter-rotating with respect to the primary bar. Maciejewski (2006, hereafter M06), more emphatically, argued that NGC 2950 has to be counter-rotating with respect to the primary. This would raise the prospect that either NGC 2950 is atypical or that counter-rotating (or possibly librating) double bars are common. However, this conclusion is based on the assumption that the TW method continues to hold for nested bars, which CDA03 suggested may not be the case.

Our simulations provide an ideal testbed for assessing the reliability of measurements of $\Omega_s$. Here we test whether the simple version of the TW method, as used by CDA03 using three slits, can recover $\Omega_s$ accurately, and check whether the signature of apparent counter-rotation can occur without actual counter-rotation.

### 5.1. The Tremaine–Weinberg Method

The TW method requires that the continuity equation be satisfied for some kinematic tracer and that the tracer's density can be written as $\Sigma(r, \phi - \Omega t)$. For slits parallel to the major axis of the disk, if $\mathcal{V}$ is the luminosity-weighted mean velocity along any such slit, and $\mathcal{X}$ the luminosity-weighted mean position along the same slit, then plotting $\mathcal{V}$ versus $\mathcal{X}$ results in a straight line with a slope of $\Omega \sin i$. This TW method has been used to measure pattern speeds in large-scale bars (Merrifield & Kuijken 1995; Gerssen et al. 1999; Debattista 2002; Aguerri et al. 2003; Gerssen et al. 2003; Debattista & Williams 2004). CDA03 showed that slits passing through the secondary bar did not lie on the same line as those passing through only the primary bar, proving that $\Omega_s \neq \Omega_p$.

CDA03 argued that while $\Omega_p$ can be measured from the region outside the secondary bar, $\Omega_s$ cannot be obtained as easily. Their reasons for this were twofold: (1) disentangling the contribution to $\mathcal{X}$ and $\mathcal{V}$ from the primary and secondary bars is non-trivial, and (2) the secondary bar cannot be in rigid rotation (Louis & Gerhard 1988; Debattista & Shen 2007), violating the assumption of the TW method that the density
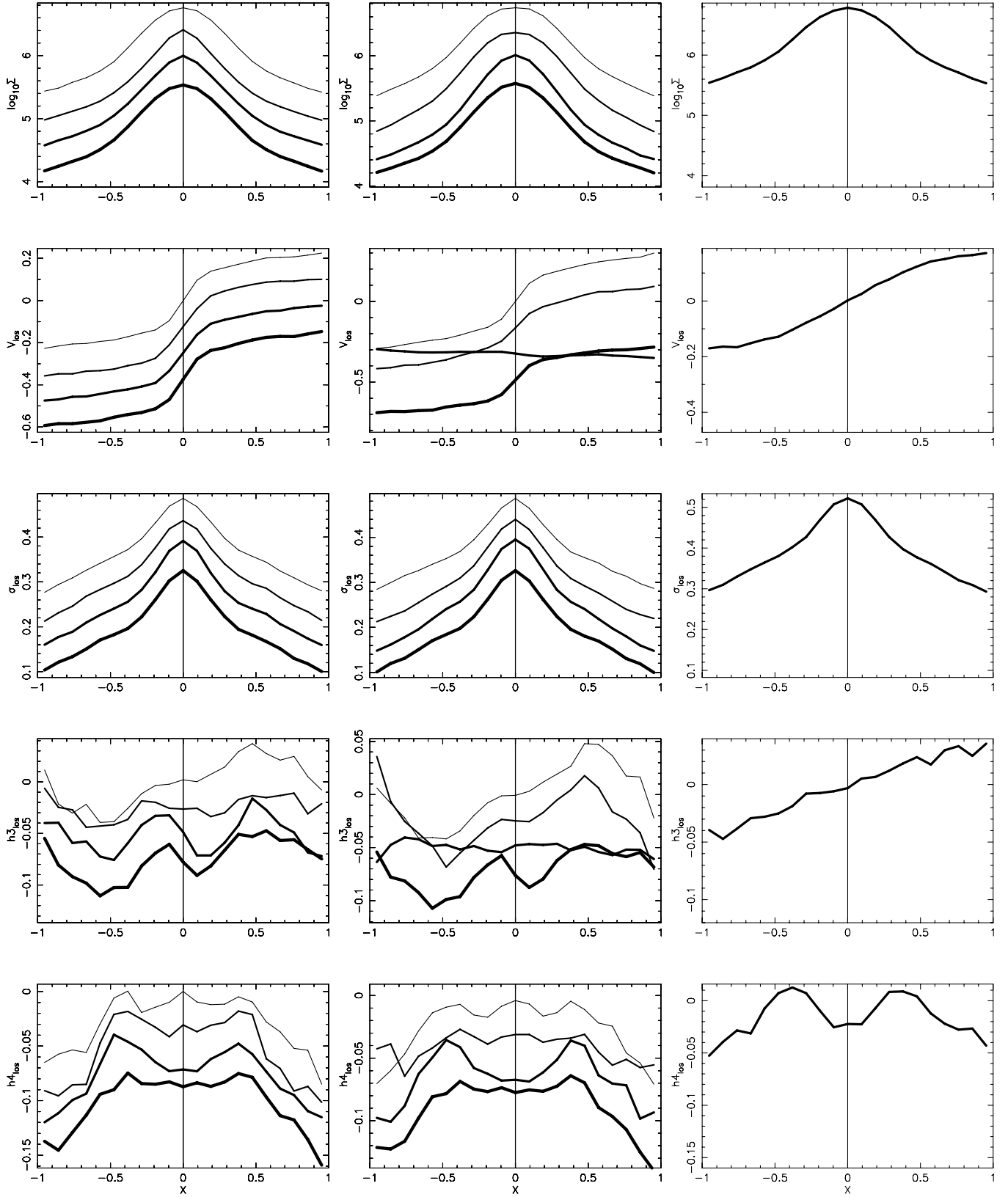
**Figure 9.** Evolution of slit profiles of runs D and S. From top to bottom panels: surface density, mean LOS velocity, velocity dispersion, $h_3$, and $h_4$. (a) Left column: slit profiles along the major axis of the *primary* bar in run D, as the secondary bar rotates through the primary one. In each panel the profiles from top to bottom with increasing line width, shifted by an arbitrary amount, represent $t = 398$ (two bars at 135°), $t = 405$ (90°), $t = 412$ (45°), and $t = 415$ ($\sim 0°$), respectively. (b) Middle column: as in (a), but slits are along the major axis of the *secondary* bar in run D. (c) Right column: as in (a), but slits are along the major axis of the (single) bar in run S at $t = 400$, which does not vary as the single bar rotates. The slit width is $\sim 0.3$ in all cases.
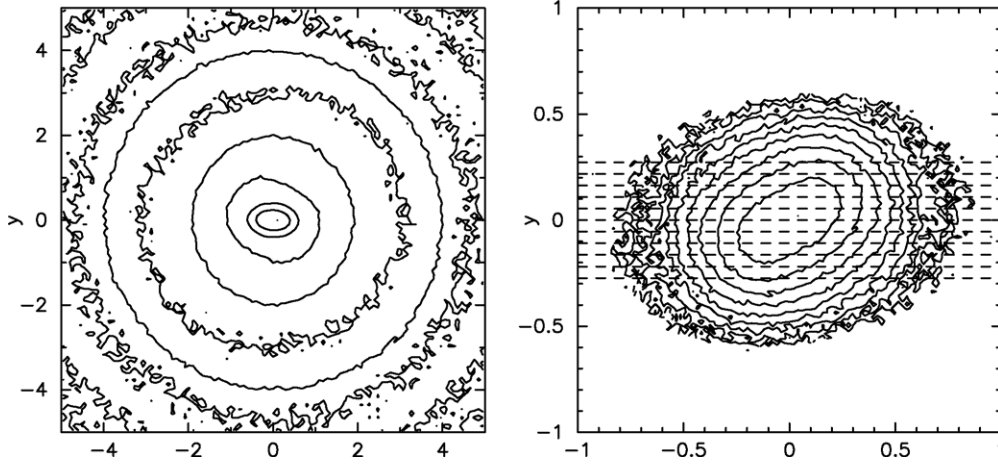
**Figure 10.** Left: the face-on surface density (disk+bulge) in run D at $t = 20$. Right: the bulge viewed at $i = 45°$ and $\psi_{nuc} = 45°$ with the slits used in the TW measurement indicated by the dashed lines.

can be expressed as $\Sigma(r, \phi - \Omega t)$. Disentangling the different contributions to integrals may be possible: CDA03 presented two models for doing this and M06 presented another. M06 also estimated the effect of non-rigid rotation to be less than 15%; this estimate was however based on the simplifying assumption that the system is two-dimensional. We therefore explore the effect of non-rigid rotation on measurements of $\Omega_s$ directly with the simulations. The novelty of our approach lies in our ability to cleanly disentangle the primary and secondary bars: in our simulations we distinguish between disk and bulge particles. While the disk particles support both the secondary and primary bars, the bulge particles almost exclusively support only the secondary bar. Thus, if we consider only bulge particles we have a quite clean tracer population for the secondary bar. It is very unlikely that any scheme that can be devised for observational data will ever be able to separate the secondary bar from the primary as cleanly as we can in our simulations.

### 5.2. Simulated TW Measurements

We therefore apply the TW method to bulge particles only. We used 11 slits covering the full region $-Y_{max} \leqslant Y \leqslant Y_{max}$, with $Y_{max} = 0.3$ where the secondary bar is strongest. This corresponds to slit widths $\delta Y = 0.055$ or $a_{B2}/\delta Y = 7.3$ (in comparison, the observations of CDA03 had $a_{B2}/\delta Y = 6.4$). We adopted an inclination $i = 45°$ and varied the secondary bar P.A. relative to the inclination axis, $\psi_{nuc}$, in the range $0° \leqslant \psi_{nuc} \leqslant 90°$. We measured $\mathcal{X}$ and $\mathcal{V}$ for each slit as in Debattista (2003, hereafter D03):

$$\mathcal{X} = \frac{1}{N_{slit}} \sum_{i \in slit} X_i, \qquad \mathcal{V} = \frac{1}{N_{slit}} \sum_{i \in slit} V_{z,i}, \qquad (1)$$

where $V_{z,i}$ and $X_i$ are the line-of-sight velocity and the $X$ coordinate of particle $i$, and $N_{slit}$ is the number of bulge particles in the slit. The sums in these definitions are over bulge particles only.

To measure $\Omega_s$ we fit a straight line to $\mathcal{V}$ as a function of $\mathcal{X}$ using least-squares. As in D03, we estimate errors on the slit integrals, $\sigma_{\mathcal{X}}$ and $\sigma_{\mathcal{V}}$, by their radial variation outside $|X| = 0.4$. We also experimented with a number of other error estimates including equal errors, the difference between positive and negative $Y$, and errors proportional to $N_{slit}$. We found that the most accurate measurements were obtained assuming weights

**Table 1**
The Results of TW Measurements

| $t$ | $\Delta\phi$ | $\Omega_s$ | $\sigma_\Omega$ |
|---|---|---|---|
| 20 | ... | 0.89 | $0.10 \pm 0.02$ |
| 398 | $135°$ | 0.42 | $0.19 \pm 0.10$ |
| 405 | $90°$ | 0.32 | $0.10 \pm 0.06$ |
| 412 | $45°$ | 0.41 | $0.17 \pm 0.12$ |
| 415 | $0°$ | 0.52 | $0.09 \pm 0.08$ |

**Note.** The column $\Delta\phi$ gives the approximate angle between the two bars.

$\sigma_{\mathcal{V}}^{-2}$, which we adopt throughout. In observations, the main uncertainties are in $\mathcal{V}$, and the linear regression is dominated by $\sigma_{\mathcal{V}}$, as here. We denote the slope of the fitted line as $\Omega_{TW} \sin i$ in order to distinguish $\Omega_{TW}$ from the pattern speed, $\Omega_s$, measured through the time evolution of the simulation. We quantify the typical errors in $\Omega_{TW}$ as

$$\sigma_\Omega = \left\langle \left| \frac{\Delta\Omega}{\Omega_s} \right| \right\rangle = \left\langle \left| 1 - \frac{\Omega_{TW}}{\Omega_s} \right| \right\rangle, \qquad (2)$$

where $\langle \rangle$ represents an average over the range $30° \leqslant \psi_{nuc} \leqslant 60°$, which are favorable orientations because they give large values of $\mathcal{X}$.

### 5.3. Precision of TW Measurements for Nuclear Bars

We start by considering the precision with which $\Omega_s$ can be measured in the absence of a primary bar by considering run D at $t = 20$, before the primary bar forms but after the nuclear bar has saturated. Figure 10 presents the surface density of the system; only a nuclear bar is present, which is well traced by the bulge particles. The right panel shows the projected surface density at $i = 45°$ and $\psi_{nuc} = 45°$ with the slits used superposed. The value of $\Omega_s$ measured from the time evolution is listed in Table 1. In Figure 11 we present the TW measurement for the same orientation. The measured $\Omega_{TW}$ is accurate to better than 10%, which is the typical uncertainty for single bars (D03; O'Neill & Dubinski 2003). The integrals $\mathcal{X}$ and $\mathcal{V}$ are both well behaved, and each pair of slits at $\pm Y$ is consistent with a single straight line that matches the pattern speed very well. Figure 12 summarizes the reliability of TW measurements for a single nuclear bar, which shows that $\Omega_s$ can be measured to better than 10% for all reasonable orientations. We also experimented with
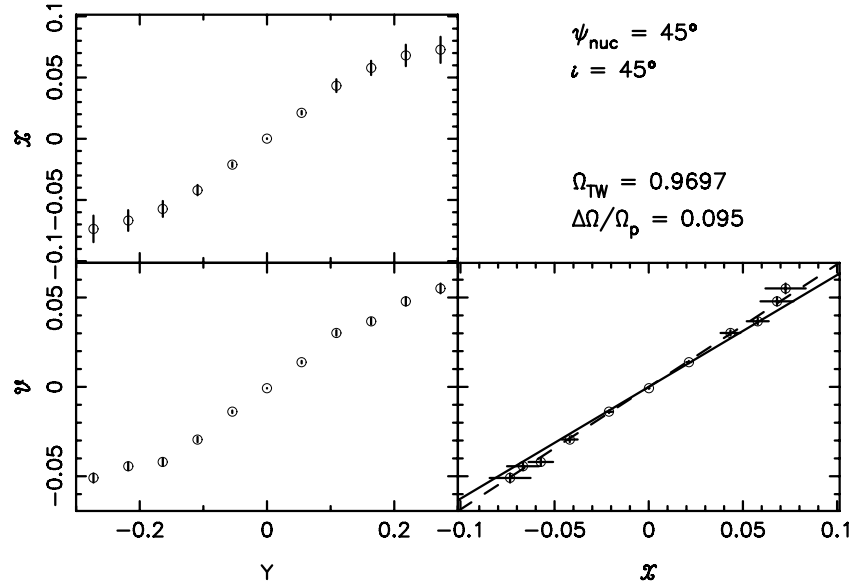
**Figure 11.** Left: the TW integrals as a function of slit offset $Y$ for run D at $t = 20$ with $i = 45°$ and $\psi_{\rm nuc} = 45°$. Right: the measurement of $\Omega_{\rm TW}$. The solid line shows $\Omega_2$ while the dashed line shows $\Omega_{\rm TW}$.
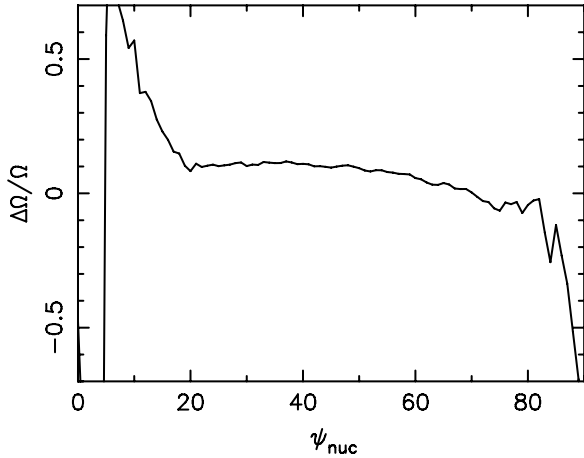


**Figure 12.** Fractional error in $\Omega_{\rm TW}$ at $t = 20$ in run D as a function of $\psi_{\rm nuc}$. The average absolute error over $30° \leqslant \psi_{\rm nuc} \leqslant 60°$ is $< 10\%$.

a three-slit configuration consisting of the central $Y = 0$ slit and $Y = \pm Y_{\rm offset}$ for each $Y_{\rm offset}$ and found $\sigma_\Omega$ increases but is still less than 14%. Thus, the TW method is well behaved for an isolated nuclear bar.

In Figure 13 we show the bulge of run D at $t = 398$–415; the secondary bar is prominent, and has insignificant or no elongation along the primary bar. Thus, using bulge particles only for TW measurements will result in only the secondary bar being included.

In Figure 14 we present a single TW measurement at $i = 45°$ and $\psi_{\rm nuc} = 45°$ for each of the four times of Figure 13. While the integrals themselves appear generally well behaved, the scatter of the points about the fitted lines is larger than at $t = 20$. This scatter leads to a larger $\sigma_\Omega$ than in the single-bar case for all orientations of the secondary bar, as shown in Figure 15 and summarized in Table 1. Other than being large at the smallest values of $|\mathcal{X}|$, $\sigma_\Omega$ does not correlate with $|\mathcal{X}|$ or $|\mathcal{V}|$. When we fit lines to three slits as before, we find that the quality of the fits varies considerably (Figure 16). The results of the same analysis on data at $t = 600$ are comparable to those at $t = 400$.

We conclude that observationally it is difficult to determine the uncertainty in any measurement of $\Omega$ based on slit data obtained by CDA03 for NGC 2950.

### 5.4. Interpretation

We have demonstrated that the standard TW method on the secondary bar, while not wholly unreliable, is unable to recover $\Omega_s$ without significant uncertainty. Observationally, this situation would be exacerbated by the need to subtract the contribution of the primary bar from the measured integrals, which we have not addressed (but see Meidt et al. 2008).

The amplitude of the $m = 2$ perturbation in bulge particles varies by some $\pm 20\%$ about the mean amplitude at all radii. Is the failure of the TW method for secondary bars consistent with the idea that non-rigid rotation leads to large errors? Evidence that this is indeed the case can be found in Figure 15, which shows the largest errors occur for $\Delta\phi = 45°$ and $\Delta\phi = 135°$. Figure 2 of Debattista & Shen (2007) shows the amplitude of the secondary bar, $A_2 \sim -\cos(2\Delta\phi)$. Thus $dA_2/dt$ peaks at $\Delta\phi = \pm 45°$, which is in excellent agreement with the phases where we find the largest errors. Moreover, the redistribution of material being radial along the secondary bar, we expect that the largest errors will occur when the radial motions contribute more to the line-of-sight velocity. While some of the error in Figure 15 is clearly due to noise at all times, a significant part is also physical. Most importantly, we find that, for $\Delta\phi = \pm 45°$, the larger $\psi_{\rm nuc}$ is, the larger is the error in $\Omega_{\rm TW}$. This leads us to conclude that, as argued by CDA03, the perturbations to the TW method due to non-rigid rotation are sufficiently large as to render simple measurements of $\Omega_2$ noisy at best.

We have focused here on using slits to compare with the observations of CDA03 and used only bulge particles to isolate the secondary bar. Meidt et al. (2008) present an analysis using an extension of the TW method which is able to disentangle multiple pattern speeds if provided full two-dimensional velocity fields. They find, as we find here, that the pattern speed of the secondary is prone to larger uncertainties. However, regularization with that method leads to more accurate measurements of $\Omega_s$.
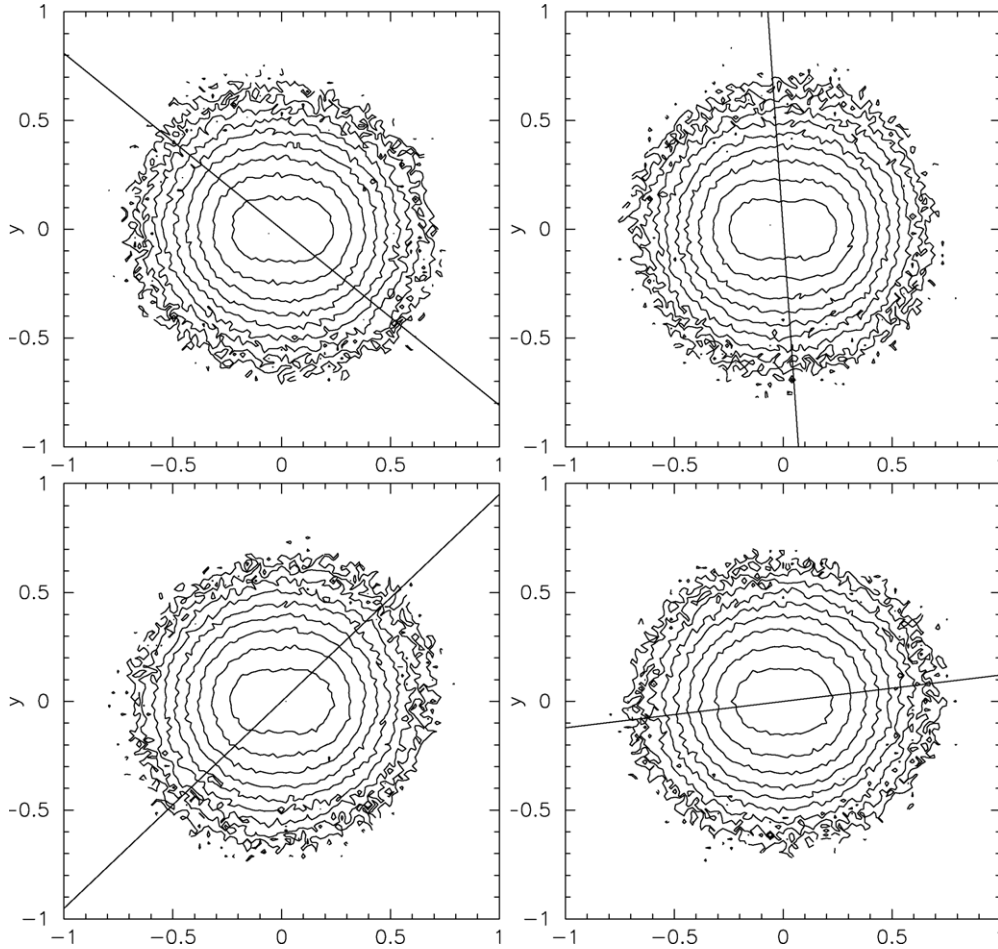
**Figure 13.** Face-on surface density of bulge particles only in run D. The different snapshots are at $t = 398$ (top left), $t = 405$ (top right), $t = 412$ (bottom left), and $t = 415$ (bottom right). The line indicates the orientation of the primary bar at the given time.

Besides the simulations presented in this paper we have also run a large number of additional simulations, which will be presented elsewhere. Among these simulations were instances in which the secondary bars experienced less variations in their amplitude. In those cases we found that the error in $\Omega_{\rm TW}$ can be significantly smaller. However, it is not obvious at present how to estimate amplitude oscillations for real systems.

### 5.5. Comparison with NGC 2950

Although we have shown that the TW method as used by CDA03 is not very accurate for secondary bars, it is not so grossly unreliable that we cannot consider the question of whether the secondary bar in NGC 2950 is counter-rotating. If it were, this would suggest a formation scenario for double-barred galaxies different from that presented here. Simulations have found that counter-rotating secondary bars are possible if counter-rotating material is present in the disk (Sellwood & Merritt 1994; Friedli 1996; Davies & Hunter 1997), and this remains a viable model if such material is present in a sufficiently large fraction of galaxies.

Starting from the assumption that both bars satisfy the continuity equation and are in rigid rotation (i.e., $\Sigma_i(R - \Omega_i t)$ for $i = s, p$), CDA03 showed that the TW method for the two bars combined becomes

$$(\mathcal{X}_p \Omega_p + \mathcal{X}_s \Omega_s) \sin i = \mathcal{V}_p + \mathcal{V}_s \equiv \mathcal{V}. \qquad (3)$$

The observed quantities are $\mathcal{V}$ and $\mathcal{X} \equiv \mathcal{X}_p + \mathcal{X}_s$, whereas the required quantities for determining the $\Omega_i$ are $\mathcal{X}_i = \int X \Sigma_i \, dX$ and $\mathcal{V}_i = \int V_{\rm los} \Sigma_i \, dX$. Since slits can be selected to pass through the primary but not the secondary bar, it is possible to derive $\Omega_p$ assuming that the oscillations in the primary are small (in good agreement with our simulations). Ignoring the effect of non-rigid rotation, CDA03 considered two assumptions for $\mathcal{X}_s$ in Equation (3) to solve for $\Omega_s$ in NGC 2950. This gave a range of possible values of $\Omega_s$, including a secondary bar counter-rotating relative to the primary bar. Using the same data, M06 made a different attempt at isolating the secondary bar. Based on his analysis, M06 also argued that the secondary bar in NGC 2950 is counter-rotating. Since the analysis of both CDA03 and M06 ignored the non-rigid rotation, neither of the estimates for $\Omega_s$ is likely to be very accurate as we showed above.

Nevertheless, we do not find in our simulations cases where the behavior of the integrals resembles that in NGC 2950. As emphasized by M06, the main characteristic of the $\mathcal{V}(Y)$ profile in NGC 2950 is that it becomes steeper without changing sign in the secondary bar region (see Figure 3 of CDA03). This happens despite the fact that the two bars are on opposite sides of the minor axis (see Figure 2), causing $\mathcal{X}_s$ to have the opposite sign of $\mathcal{X}_p$ and leading to $|\mathcal{X}|$ declining more rapidly in the secondary bar region. But instead of $\mathcal{V}$ also being shallower in this region, CDA03 found that $\mathcal{V}(Y)$ steepens there. For TW measurements of the system in Figure 2, a TW measurement
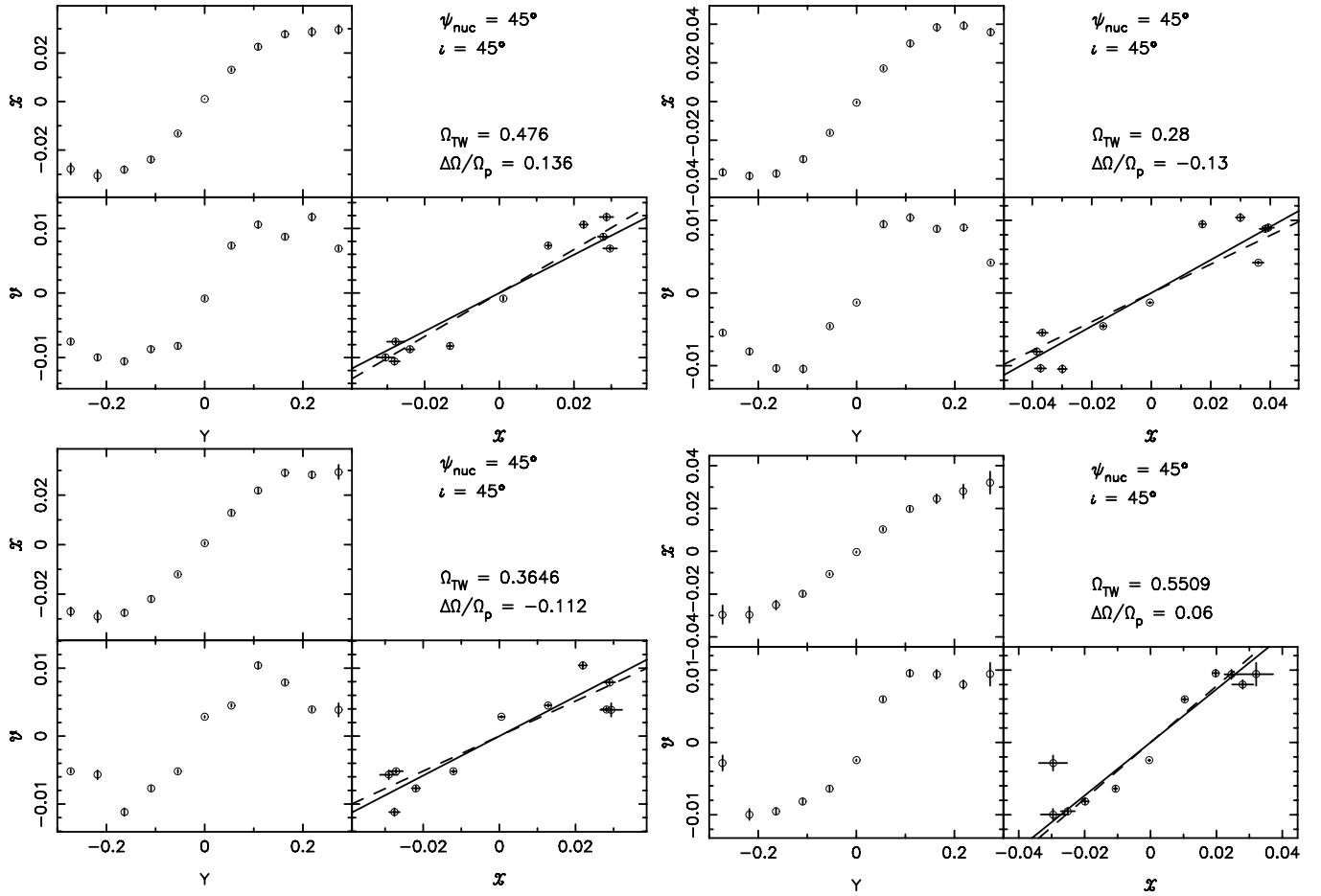
**Figure 14.** TW measurements with $i = 45°$ and $\psi_{\rm nuc} = 45°$ at $t = 398$ (top left), $t = 405$ (top right), $t = 412$ (bottom left), and $t = 415$ (bottom right). The solid lines show $\Omega_2$ while the dashed lines show $\Omega_{\rm TW}$.
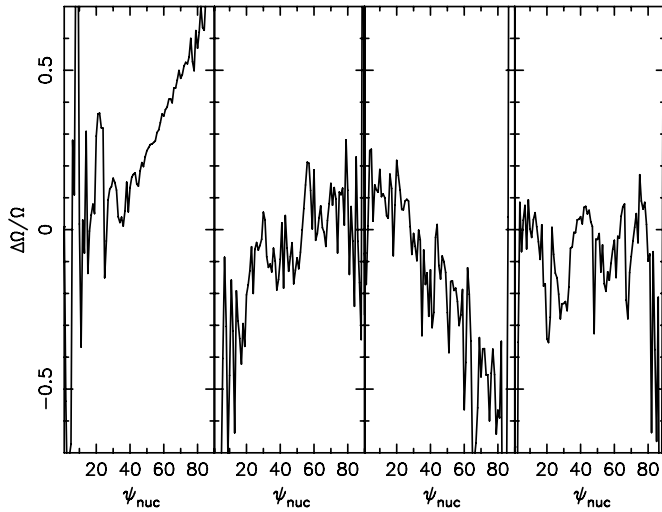


**Figure 15.** Full TW analysis for bulge particles only in run D. The different panels are at $t = 398$, $t = 405$, $t = 412$, and $t = 415$, respectively (from left to right).



**Figure 16.** Precision of TW measurements of secondary bars in nine models using three slits as described in the text. The different points are offset horizontally for clarity. The colors indicate $t = 20$: black, $\psi_{\rm nuc} \simeq 135°$: blue ($t = 398$ and $t = 593$), $\psi_{\rm nuc} \simeq 90°$: green ($t = 405$ and $t = 599$), $\psi_{\rm nuc} \simeq 45°$: yellow ($t = 412$ and $t = 605$), and $\psi_{\rm nuc} \simeq 0°$: red ($t = 415$ and $t = 609$). The error bars on the individual points show the $1\sigma$ variations in the interval $30° \leqslant \psi_{\rm nuc} \leqslant 60°$.

(A color version of this figure is available in the online journal.)

using slits passing through both bars (now with both disk and bulge particles included) does not show a steeper $\mathcal{V}(Y)$ profile (see Figure 17). We conclude that NGC 2950 may indeed have counter-rotating primary and secondary bars. Another possibility might be that the secondary bar librates about the primary bar, which deserves more investigation in future studies.
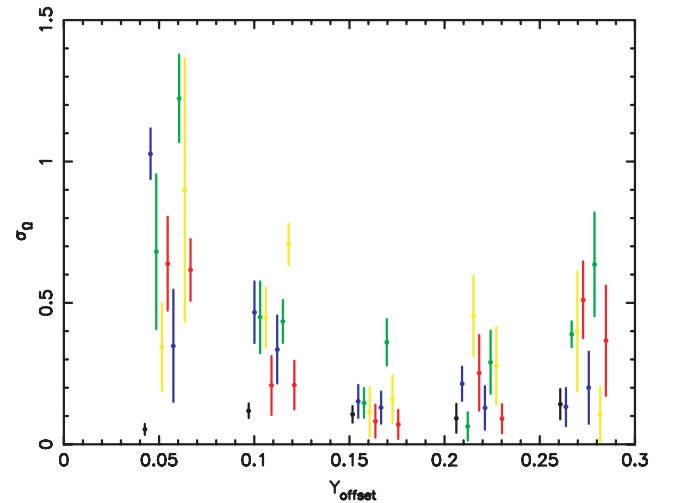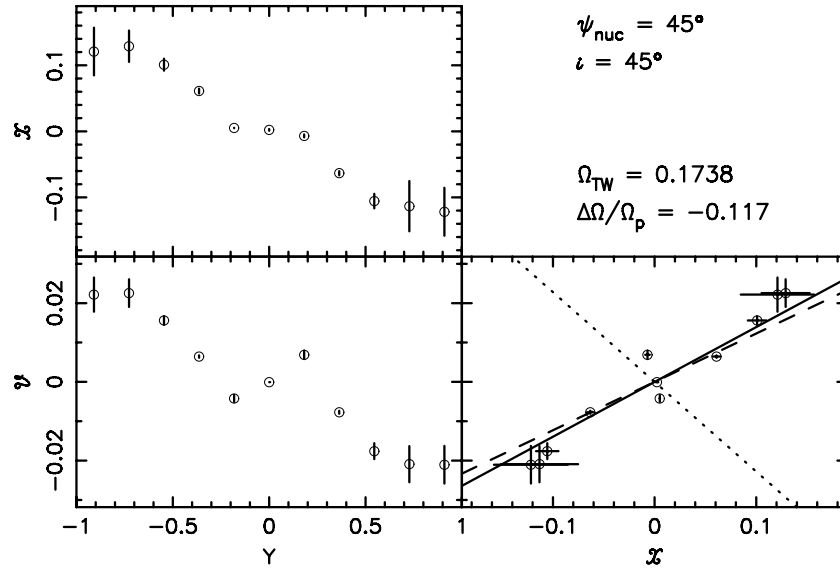
**Figure 17.** TW measurement for the full system of bulge+disk at $t = 405$ shown in Figure 2. The solid line is for $\Omega_p$ while the dotted line is for $-\Omega_s$. The best-fit straight line to the points is shown by the dashed line. The relative weights of bulge particles (their "mass-to-light" ratio) have been adjusted to roughly reproduce $\mathcal{X}(Y)$ in NGC 2950. This figure is to be compared with Figure 3 of CDA03.

## 6. CONCLUSIONS

We have analyzed the photometric and kinematic properties of our high-resolution models, and contrasted them when with or without a secondary bar. This study also compared the simulated secondary bars with observations.

In general, the shape of secondary bars in our models is reasonable compared to those observed. The length ratio of two bars, determined by various methods, is in the range 0.12–0.19, in good agreement with Erwin & Sparke (2002, 2003). We also found the overall edge-on shape of boxy bulges is largely unaffected by the existence of a secondary bar. At lower inclinations, the central density profile along the primary bar major axis is lower than that along the minor axis, due to the secondary bar orienting to a different direction.

The primary extends roughly to its CR, and therefore fits the definition of a fast bar (see, e.g., Aguerri et al. 2003). Although the secondary bar rotates more rapidly than the primary, its semimajor axis is much shorter than its CR, even if we take the oscillation of the speeds of bar patterns into account. We did not find evidence of CR–ILR coupling (e.g., Pfenniger & Norman 1990; Friedli & Martinet 1993) in our models.

We find that the central twist of the kinematic axis is quite weak, even if a secondary bar is present, due to the relatively large velocity dispersion of stars in the central region. This is consistent with the two-dimensional stellar kinematics of secondary bars studied in Moiseev et al. (2004). Another kinematic feature often present in our double-barred models is a ring-like feature in the fourth-order Gauss–Hermite moment $h_4$ maps. An $h_3$ reversal feature may also appear in the nuclear region at some favorable orientations and times. We do not find a velocity dispersion $\sigma$-drop for our secondary bar model. It is more likely that $\sigma$-drops are just the signature of newly formed stars, and are not necessarily a unique feature of double-barred systems.

We showed that the TW method is not very reliable even when the primary bar contribution is fully excluded. The way in which the measurement fails is consistent with the proposal of CDA03, namely that the non-rigid rotation leads to internal motions that violate the stationary frame assumption of the method. Nonetheless, we find no example in our simulations where the behavior of the TW integrals mimics that observed in NGC 2950. Thus, this galaxy may indeed have counter-rotating secondary and primary bars.

The general agreement between our simulations and observations of double-barred galaxies gives us confidence that the simulations are capturing the same dynamics as in nature. This is especially remarkable because secondary bars are not merely scaled down versions of primary bars, but have distinctly different kinematic properties. In the absence of self-consistent simulations, earlier orbit-based models could not directly confront the challenge from observations which found such differences. This demonstrates the advantage of finally being able to simulate stellar double-barred galaxies, which had been puzzling for so long.

## REFERENCES

Aguerri, J. A. L., Debattista, V. P., & Corsini, E. M. 2003, MNRAS, 338, 465
Athanassoula, E., & Beaton, R. L. 2006, MNRAS, 370, 1499
Bender, R., Saglia, R. P., & Gerhard, O. E. 1994, MNRAS, 269, 785
Binney, J. 1978, MNRAS, 183, 501
Bureau, M., & Athanassoula, E. 2005, ApJ, 626, 159
Buta, R., & Crocker, D. A. 1993, AJ, 105, 1344
Combes, F., Debbasch, F., Friedli, D., & Pfenniger, D. 1990, A&A, 233, 82
Corsini, E. M., Debattista, V. P., & Aguerri, J. A. L. 2003, ApJ, 599, L29
Davies, C. L., & Hunter, J. H. 1997, ApJ, 484, 79
Debattista, V. P. 2003, MNRAS, 342, 1194
Debattista, V. P., Carollo, C. M., Mayer, L., & Moore, B. 2005, ApJ, 628, 678
Debattista, V. P., Corsini, E. M., & Aguerri, J. A. L. 2002, MNRAS, 332, 65
Debattista, V. P., Mayer, L., Carollo, C. M., Moore, B., Wadsley, J., & Quinn, T. 2006, ApJ, 645, 209
Debattista, V. P., & Sellwood, J. A. 2000, ApJ, 543, 704
Debattista, V. P., & Shen, J. 2007, ApJ, 654, L127
Debattista, V. P., & Williams, T. B. 2004, ApJ, 605, 714
de Vaucouleurs, G. 1975, ApJS, 29, 193
Emsellem, E., Fathi, K., Wozniak, H., Ferruit, P., Mundell, C. G., & Schinnerer, E. 2006, MNRAS, 365, 367

Emsellem, E., Greusard, D., Combes, F., Friedli, D., Leon, S., Pécontal, E., & Wozniak, H. 2001, A&A, 368, 52
Erwin, P. 2004, A&A, 415, 941
Erwin, P. 2005, MNRAS, 364, 283
Erwin, P., & Sparke, L. S. 2002, AJ, 124, 65
Erwin, P., & Sparke, L. S. 2003, ApJS, 146, 299
Friedli, D. 1996, A&A, 312, 761
Friedli, D., & Martinet, L. 1993, A&A, 277, 27
Gerhard, O. E. 1993, MNRAS, 265, 213
Gerssen, J., Kuijken, K., & Merrifield, M. R. 1999, MNRAS, 306, 926
Gerssen, J., Kuijken, K., & Merrifield, M. R. 2003, MNRAS, 345, 261
Heller, C. H., Shlosman, I., & Athanassoula, E. 2007a, ApJ, 657, L65
Heller, C. H., Shlosman, I., & Athanassoula, E. 2007b, ApJ, 671, 226
Kormendy, J., & Kennicutt, R. C. 2004, ARA&A, 42, 603
Lisker, T., Debattista, V. P., Ferreras, I., & Erwin, P. 2006, MNRAS, 370, 477
Louis, P. D., & Gerhard, O. E. 1988, MNRAS, 233, 337
Lynden-Bell, D. 1962, MNRAS, 123, 447
Maciejewski, W. 2006, MNRAS, 371, 451
Maciejewski, W., & Athanassoula, E. 2007, MNRAS, 380, 999
Maciejewski, W., & Sparke, L. S. 1997, ApJ, 484, L117
Maciejewski, W., & Sparke, L. S. 2000, MNRAS, 313, 745
Marinova, I., & Jogee, S. 2007, ApJ, 659, 1176
Martinez-Valpuesta, I., Shlosman, I., & Heller, C. 2006, ApJ, 637, 214

Meidt, S. E., Rand, R. J., Merrifield, M. R., Debattista, V. P., & Shen, J. 2008, ApJ, 676, 899
Menéndez-Delmestre, K., Sheth, K., Schinnerer, E., Jarrett, T. H., & Scoville, N. Z. 2007, ApJ, 657, 790
Merrifield, M. R., & Kuijken, K. 1995, MNRAS, 274, 933
Moiseev, A. V., Valdés, J. R., & Chavushyan, V. H. 2004, A&A, 421, 433
O'Neill, J. K., & Dubinski, J. 2003, MNRAS, 346, 251
Petitpas, G. R., & Wilson, C. D. 2002, ApJ, 575, 814
Petitpas, G. R., & Wilson, C. D. 2004, ApJ, 603, 495
Pfenniger, D., & Norman, C. 1990, ApJ, 363, 391
Prendergast, K. H., & Tomer, E. 1970, AJ, 75, 674
Raha, N., Sellwood, J. A., James, R. A., & Kahn, F. D. 1991, Nature, 352, 411
Rautiainen, P., Salo, H., & Laurikainen, E. 2002, MNRAS, 337, 1233
Schinnerer, E., Maciejewski, W., Scoville, N., & Moustakas, L. A. 2002, ApJ, 575, 826
Sellwood, J. A., & Merritt, D. 1994, ApJ, 425, 530
Sellwood, J. A., & Valluri, M. 1997, MNRAS, 287, 124
Shen, J., & Sellwood, J. A. 2004, ApJ, 604, 614
Shlosman, I., Frank, J., & Begelman, M. C. 1989, Nature, 338, 45
Tremaine, S., & Weinberg, M. D. 1984, ApJ, 282, L5
van Albada, T. S., & Sanders, R. H. 1982, MNRAS, 201, 303
van der Marel, R. P., & Franx, M. 1993, ApJ, 407, 525
Wozniak, H., & Champavert, N. 2006, MNRAS, 369, 853
Wozniak, H., Combes, F., Emsellem, E., & Friedli, D. 2003, A&A, 409, 469